













Spectrophotometric Analysis of the Ryugu Rock Seen by MASCOT: Searching for a Carbonaceous Chondrite Analog

Stefan Schröder¹ , Katharina Otto¹ , Hannah Scharf¹, Klaus-Dieter Matz¹, Nicole Schmitz¹ , Frank Scholten¹ , Stefano Mottola¹ , Frank Trauthan¹, Alexander Koncz¹ , Harald Michaelis¹, Ralf Jaumann¹ , Tra-Mi Ho² , Hikaru Yabuta³ , and Seiji Sugita⁴ 

¹ Deutsches Zentrum für Luft- und Raumfahrt (DLR), Institute of Planetary Research, D-12489 Berlin, Germany; stefanus.schroeder@dlr.de

² Deutsches Zentrum für Luft- und Raumfahrt (DLR), Institute of Space Systems, D-28359 Bremen, Germany

³ Hiroshima University, Department of Earth and Planetary Systems Science, 739-8526 Hiroshima, Japan

⁴ University of Tokyo, Department of Earth and Planetary Science, 113-0033 Tokyo, Japan

Received 2020 July 20; revised 2020 September 22; accepted 2020 September 23; published 2021 March 16

Abstract

We analyze images of a rock on Ryugu acquired in situ by MASCam, the camera on the MASCOT lander, with the aim of identifying possible carbonaceous chondrite (CC) analogs. The rock's reflectance ($r_F = 0.034 \pm 0.003$ at phase angle $4.5^\circ \pm 0.1^\circ$) is consistent with Ryugu's average reflectance, suggesting that the rock is typical for this asteroid. A spectrophotometric analysis of the rock's inclusions provides clues to its CC group membership. Inclusions are generally brighter than the matrix. The dominant variation in their color is a change in the visible spectral slope, with many inclusions being either red or blue. Spectral variation in the red channel hints at the presence of the $0.7 \mu\text{m}$ absorption band linked to hydrated phyllosilicates. The inclusions are unusually large for a CC; we find that their size distribution may best match that of the Renazzo (CR2) and Leoville (CV3) meteorites. The Ryugu rock does not easily fit into any of the CC groups, consistent with the idea that typical Ryugu-type meteorites are too fragile to survive atmospheric entry.

Unified Astronomy Thesaurus concepts: [Carbonaceous chondrites \(200\)](#); [Asteroids \(72\)](#); [Near-Earth objects \(1092\)](#); [Small solar system bodies \(1469\)](#); [Surface photometry \(1670\)](#); [Planetary surfaces \(2113\)](#); [Surface composition \(2115\)](#)

1. Introduction

On 2018 October 3, MASCOT was released by the Hayabusa2 spacecraft to land on the small near-Earth asteroid 162173 Ryugu (Ho et al. 2017). Hayabusa2 characterized Ryugu as a dark, moderately hydrated rubble pile, the product of the violent disruption of an undifferentiated, aqueously altered parent body (Kitazato et al. 2019; Sugita et al. 2019). Data acquired by MASCOT during its 17 hour mission revealed the surface of this C-type asteroid in unprecedented detail. Three scientific instruments collected valuable data. The MASCam camera acquired a total of 120 images, 65 of which show Ryugu's surface (Jaumann et al. 2019). Images acquired during the descent show rocks and boulders of diverse morphology but no deposits of fine-grained material. MASCam was equipped with light-emitting diodes (LEDs) in four colors, covering the visible wavelength range to the near-infrared, to allow imaging at night. Close-up night-time imaging of a small rock in front of the lander revealed abundant multicolored inclusions set in a dark matrix that resemble those in chondritic meteorites. MASCam images of the landing site allowed the construction of a digital terrain model (DTM; Scholten et al. 2019). The MARA radiometer had a good view of the rock imaged by MASCam and determined that it had a low thermal inertia, consistent with a high porosity and low tensile strength (Grott et al. 2019). The MARA data are incompatible with the presence of an optically thick dust layer on the surface of the rock. The rock's low strength suggests that a Ryugu-type meteorite may not survive atmospheric entry. The Hayabusa2

thermal infrared imager confirmed that the majority of boulders on Ryugu are highly porous, with only a minority being as dense as typical carbonaceous chondrites (CCs; Okada et al. 2020). The MasMag magnetometer found that Ryugu has no detectable magnetization, which suggests that its parent body did not possess a dynamo (Herčík et al. 2020). MASCOT's fourth instrument, the MicrOmega near-IR spectrometer (Bibring et al. 2017), appears not to have acquired useful data. Thus, only MASCam performed an in situ spectral characterization of Ryugu's surface.

Observations from orbit provided a clear link between the Ryugu surface and CC meteorites (Kitazato et al. 2019; Sugita et al. 2019; Okada et al. 2020). The inclusions seen in the MASCam images support the idea that the Ryugu rock is akin to the CCs (Jaumann et al. 2019). The question now is whether we have meteorite analogs of Ryugu in our collections. Sugita et al. (2019) argued, on the basis of their low reflectance over the visible range, that aqueously altered and thermally metamorphosed meteorites (ATCCs) are good analogs. The Ryugu spectrum has a weak and narrow absorption feature at $2.7 \mu\text{m}$ that is characteristic of OH-bearing minerals. Kitazato et al. (2019) found that Ivuna (CI1) heated to 500°C (i.e., an artificial ATCC) is a good match for Ryugu in terms of overall reflectance and $2.7 \mu\text{m}$ band strength and shape. Jaumann et al. (2019) proposed the Tagish Lake meteorite as a possible Ryugu analog. Tagish Lake is a CC of unusually low density that defies straightforward spectral classification; it bears similarities to the CI1 and CM groups, but is distinct from both (Zolensky et al. 2002). Its reflectance is unusually low in the visible wavelength range (Hiroi et al. 2001; Cloutis et al. 2012c), and, unlike typical CI meteorites, it has abundant inclusions (Zolensky et al. 2002). All these properties make it an attractive analog candidate.



Original content from this work may be used under the terms of the [Creative Commons Attribution 4.0 licence](#). Any further distribution of this work must maintain attribution to the author(s) and the title of the work, journal citation and DOI.

Table 1
Image Sets Acquired During the Two Nights on Ryugu

Night	Set	Location	ID	T (°C)
1	5	MP1a	350–355	30
1	6	MP1a	400–405	27
1	7	MP1a	450–455	17
1	8	MP1a	450–455	10
1	9	MP1b	450–455	4
2	11	MP2b	650–655	26
2	12	MP2c	700–705	14
2	13	MP2c	750–755	5
2	14	MP2c	750–755	−4
2	15	MP2c	750–755	−11

Note. ID refers to image number, T is the detector temperature, and locations are from Scholten et al. (2019). The image ID is not unique for acquisition sequences that were repeated.

This article extends the preliminary investigation of the Ryugu rock by Jaumann et al. (2019), with special focus on the spectrophotometric properties and size distribution of the inclusions. We improved the calibration of the MASCAM images where it proved challenging to properly account for the peculiarities of the LED light source. Our aim is to find the best meteorite analog of Ryugu based on information we can retrieve from the close-up images, i.e., inclusion color, abundance, and absolute reflectance. Even if we do not have Ryugu analogs in our collections, we can learn much from a detailed comparison of the Ryugu rock with various carbonaceous chondrite groups. Our analysis also addresses the question of how diagnostic close-up, multispectral images are for the physical characteristics of the asteroid surface. Until we recover the Hayabusa2 samples of Ryugu’s surface (Sawada et al. 2017), the MASCAM images represent the highest resolution observations of C-type asteroid material.

2. Methods

2.1. Data Selection

The analysis in this paper concerns night-time images that show the surface of Ryugu in reflected LED light. MASCOT spent two nights on Ryugu. Images from the first night show only the night sky, but images from the second night show a rock in clear detail. Table 1 lists all image sets acquired by MASCAM during these two nights. Five image sets (#11–15) were acquired in the second night. The first set (11) was taken at dusk and shows rocks in the background still illuminated by the Sun. The last set (15) was taken at early dawn and some images show evidence of daylight in the top right corner, a potential source of stray light. The three remaining sets (12, 13, and 14) are suitable for spectrophotometric analysis. These sets consist of six images: one bias image, one dark image, and one image for each LED color (Table 2). A bias image has the smallest available exposure time of 0.2138 ms. Set 14 is of especially good quality because it was acquired at subzero temperatures, for which detector dark current was negligible (Jaumann et al. 2017).

The images of the empty sky from the first night were expected to be mostly devoid of signal, but instead show LED stray light that may be internal to the optics. It was not noticed

Table 2
Details of the Images in Set 13, 14, and 15 in Order of Acquisition

ID	LED	t_{exp} (ms)
750	...	962.1000
751	red	2946.3778
752	green	2946.3778
753	blue	2946.3778
754	infrared	2946.3778
755	...	0.2138

before launch but was subsequently identified in images acquired on ground. We used the images from the first night to construct stray light patterns for the purpose of calibration. First, we calibrated the images from sets 7 and 8 by subtracting bias and dark current and applying the nonlinearity correction (Jaumann et al. 2017). The bulk dark current was very low, but the presence of many relatively hot pixels made a correction necessary. We then constructed a stray light pattern for each LED color as the average of the two calibrated images (one from either set). The final stray light patterns shown in Figure 1 have been convolved by a Gaussian kernel 9×9 pixels in size with a FWHM of 3 pixels to reduce noise. The patterns show that stray light in the image center is strongest for the blue LED and that the infrared LEDs cause strong stray light in the upper right corner.

2.2. Radiometric Calibration

The LED images of sets 13, 14, and 15 (all numbered #751–754) were calibrated as described in Jaumann et al. (2017) with a few modifications. The first step is to produce a clean image by subtracting the bias image (#755) and applying the nonlinearity correction (Jaumann et al. 2017). While a dark image was acquired (#750), we omitted the step of correcting for dark current because the low temperature made dark current negligible. We verified that the dark current image contained only noise; subtracting it in an effort to correct for dark current merely increased the noise in the calibrated image. The resulting clean images C_i (images are denoted in bold) were calibrated to radiance in $\text{W m}^{-2} \text{sr}^{-1}$ as

$$L_i = \frac{C_i/t_{\text{exp}} - S_i}{R_i V_i}, \quad (1)$$

with the exposure time t_{exp} in ms, responsivity factors R_i in ($\text{m}^2 \text{sr mJ}^{-1}$), and color ratio frames V_i (see below). Index i indicates the LED color (Table 3). In this paper, we refer to (L_1, L_2, L_3, L_4) as (B, G, R, I) , corresponding to the blue, green, red, and infrared radiance images. Ideally, correcting for differences in irradiance between the LEDs of different colors is done when converting radiance to reflectance. But as the LED irradiance critically depends on topography (which is not accurately known over the entire field of view), dividing by the ratio frames in Equation (1) ensures that color composites constructed from radiance images are correctly balanced. The stray light images S_i , described in the previous section have the unit DN ms^{-1} . Figure 2 shows that the stray light correction is substantial for the Ryugu images. Because we also identified

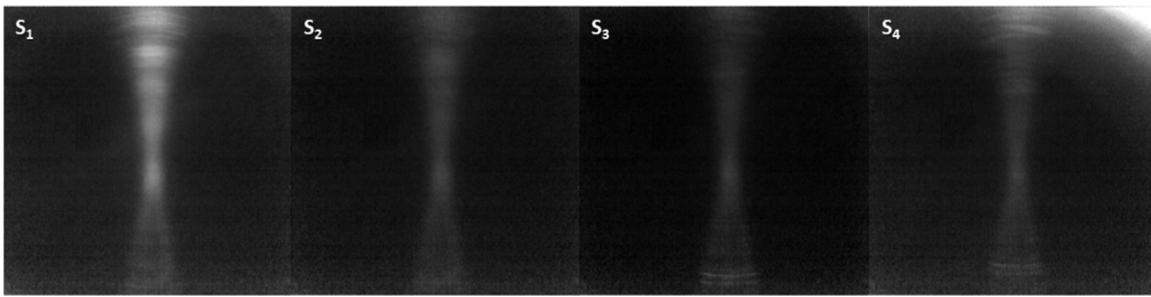


Figure 1. Stray light patterns for all LED colors, shown with identical brightness stretch (black is zero signal).



Figure 2. LED stray light correction for the (red, green, blue) = (I, G, B) composite of set 14. Left: without correction. Right: with correction. The brightness of both composites is enhanced identically.

stray light in older images that were used to derive the responsivity factors R_i in Jaumann et al. (2017), we re-derived the factors from those images with stray light subtracted (Table 3). The correction is minor, only 2% at most. The LEDs were regularly monitored during the cruise phase and were found to be stable. The revised factors are listed in Table 3. The exposure time of the LED images in sets 13, 14, and 15 was rather long, at almost 3 seconds, as the auto-exposure algorithm (Jaumann et al. 2017) successfully compensated for the relatively large distance to the dark rock. Only a handful of pixels, inside the brightest inclusions, were overexposed. Overexposure is defined as an image pixel having a signal larger than 12.5 kDN after bias subtraction. Because the nonlinearity correction fails for such high values (Jaumann et al. 2017), overexposed pixels were excluded from the analysis. For set 14, the number of overexposed pixels is 2 in the blue image, 5 in the green image, and 37 in the red image. No pixels were overexposed in the infrared image because of the comparatively low LED flux at this wavelength.

The Ryugu rock color composite shown in Jaumann et al. (2019) features an obvious calibration artifact in the form of a green bar at the bottom. The images in this composite had been calibrated using the color ratio frames V_i as constructed from images of a barium sulfate plate in the nominal landing configuration, i.e., parallel to the bottom side of both MASCOT and the camera. In reality, MASCOT did not come to rest on a

Table 3
Revised Responsivity Factors R_i for the LED Colors

i	LED	λ_{eff} (nm)	R ($\text{m}^2 \text{sr mJ}^{-1}$)
1	blue	471_{-16}^{+6}	109.7 ± 1.2
2	green	532_{-24}^{+12}	130.7 ± 1.3
3	red	630_{-7}^{+10}	127.3 ± 1.4
4	infrared	809_{-17}^{+18}	95.4 ± 1.3

Note. The range for the effective wavelength λ_{eff} is the FWHM.

flat surface. Fortunately, we had also acquired images of the plate tilted at various angles prior to launch in anticipation of such an occurrence. Figure 3 shows the calibrated green image G_p of the plate tilted forward at an angle of 30° with respect to the plane parallel to the bottom of the camera (plate images are indicated with the subscript “p”). This configuration better matches both the distance and orientation of the Ryugu rock with respect to MASCAM. Calibrating the plate images included a correction for stray light. The figure also shows a map of the distance to the plate surface, which can be compared to the map of the distance to the Ryugu surface which we will introduce in the following section. We were able to accurately derive the distance to the plate from images of a chessboard pattern that was positioned at the same distance and tilt angle as

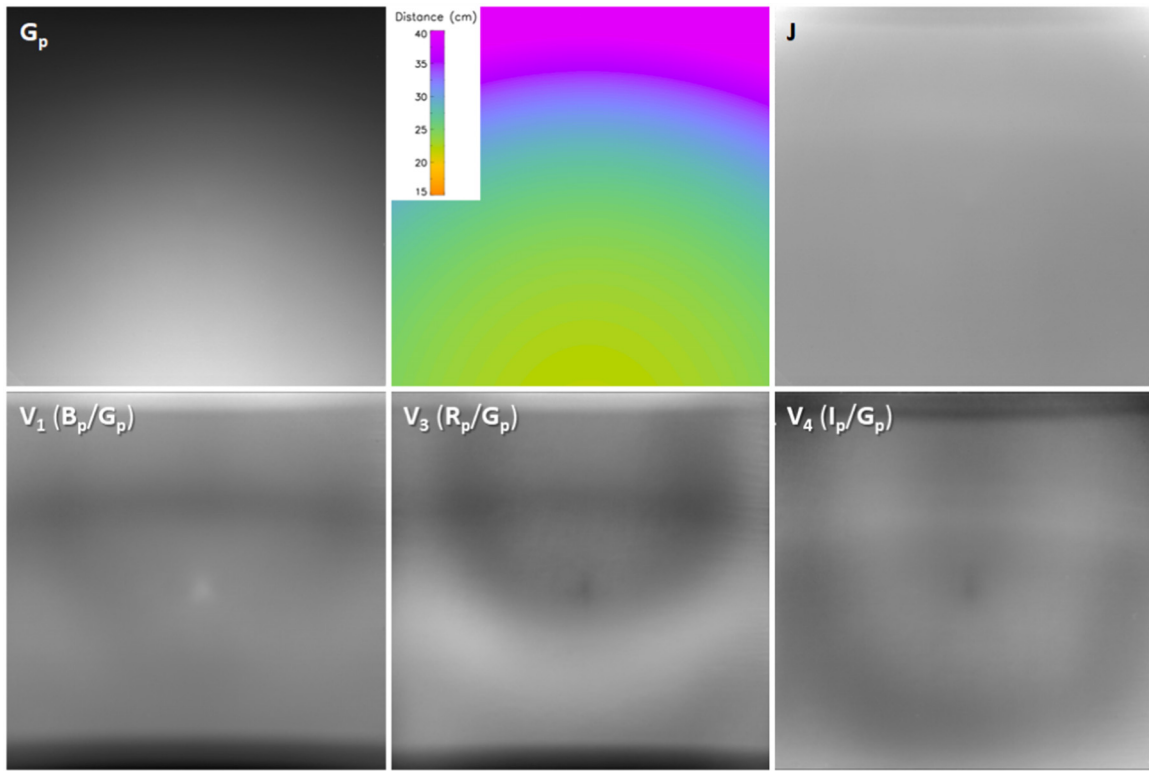


Figure 3. Color ratio frames V_i were constructed from images of a BaSO_4 plate inclined by 30° from the horizontal plane. The top row shows the green image of the illuminated plate (G_p , black is zero), the distance from the camera aperture to the plate surface, and the irradiance image J derived from G_p (black is zero). The bottom row shows the ratio frames, whose brightness is stretched such that $\pm 30\%$ of the median is white and black, respectively.

the plate. From the tilted plate images we constructed the new ratio frames V_i in Figure 3, which are defined with respect to the green image as $V_1 = B_p/G_p$, $V_2 = 1$, $V_3 = R_p/G_p$, and $V_4 = I_p/G_p$. The ratio frames are normalized at a location near the image center for which the responsivities in Table 3 were derived. Division as in Equation (1) ensures that the barium sulfate plate would appear white in a color composite of radiance images, at least at the location of normalization. In addition, the irradiance J in (W m^{-2}) of the green LEDs at unit distance could be determined from G_p , where we assumed that the plate has Lambertian reflective properties. For this, we calculated the distance from the center of the LED array to the plate surface and the incidence angle of the light on the plate coming from the same direction, where we used the fact that the LED array is located 1.8 cm below the aperture. The irradiance image J in Figure 3 appears homogeneous over most of the frame, as expected. The irradiance apparently increases toward the top corners, which is likely an artifact resulting from the LED array being extended rather than a point source and/or non-Lambertian reflective properties of the plate. We judge the irradiance image to be reliable in the bottom half of the frame. Knowing the irradiance allows us to estimate Ryugu's absolute reflectance (radiance factor, I/F) in image pixel (x, y) as

$$(r_F)_{x,y}^i = \pi \frac{d_{x,y}^2 I_{x,y}^i}{d_{\text{ref}}^2 J_{x,y}}, \quad (2)$$

with d the distance from the center of the LED array to the Ryugu surface in centimeters and reference distance $d_{\text{ref}} = 1$ cm.

The impact of the color correction (division by the ratio frames V_i in Equation (1)) on the calibration to radiance is

shown in Figure 4. Here, we compare color composites of uncorrected radiance images, images corrected with the earlier set of ratio frames, and images corrected with the revised frames in Figure 3. The revised frames successfully prevent the green bar at the bottom from appearing on the surface close to the camera. The origin of the green bar lies in the obscuration of the bottom row of LEDs on the array by the physical structure surrounding the array. The bottom row has only red and blue LEDs (Figure 5), and therefore the bar at the bottom of the image for terrain that is close to the camera is green (and IR). Where the terrain is more distant (the apparent hollow at the bottom right), the green bar is still faintly visible. This illustrates the difficulty in calibrating images of a surface that is illuminated by this LED device, which has an illumination pattern that is different for each color and, moreover, depends on the distance to the surface. Other artifacts apparently remain in the images after calibration. One way to identify calibration artifacts is to construct ratios of the LED color images. Figure 6 shows three such ratios: G/B , R/G , and I/R . Both the G/B and R/G ratios shows traces of the green bar artifact at the bottom of the frame, but only for the more distant terrain. The G/B ratio shows a darkening in the center of the frame that may indicate a slight overcorrection of stray light. The R/G ratio shows bright vertical stripes at the left of the frame that represent an excess of red signal. This pattern, which had not been seen before, is probably stray light. The stripes are also faintly visible in the G/B ratio. The I/R ratio frame is relatively dark in the center. We suspect that this is not related to the reflective properties of the rock but to the illumination pattern of the infrared LEDs being different from that expected (i.e., an incorrect V_4). Contours of rock topography are clearly visible in all ratio frames, either in black or white. This artifact



Figure 4. Color correction of the (red, green, blue) = (R , G , B) composite of set 14 (brightness enhanced). Left: no color correction ($V_i = 1$). Middle: colors corrected using the V_i in Figure 19 in Jaumann et al. (2017). Right: colors corrected using the V_i in Figure 3.

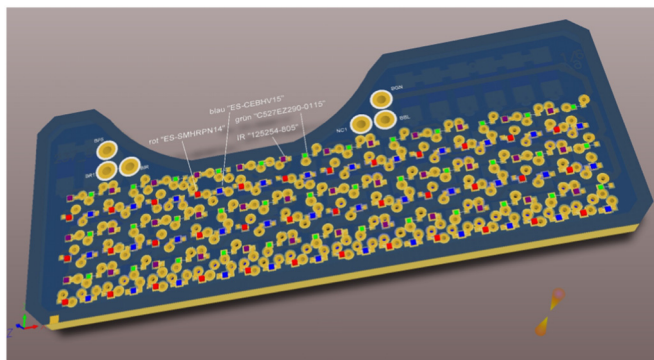


Figure 5. CAD drawing of the MASCam LED array showing the distribution of the four colors: blue, green, red, and IR.

also results from the arrangement of colors over the LED array (Figure 5). In this case, the terrain was illuminated by the top row of the array (green and IR), while from the perspective of the second row from the top (red and blue) it was in the shadow. This is consistent with the contours showing as white in the G/B and I/R ratio frames.

2.3. Inclusion Mapping

Inclusions were mapped in the radiance (R , G , B) color composite of set 14 at its full brightness range using the ArcGIS⁵ mapping tools. One of us (H.S.) did the mapping to achieve consistent results. Inclusions were identified as areas of different brightness or color compared to their immediate surroundings (“matrix”). They were outlined by drawing a polygon between the pixels of highest color and brightness contrast at a constant zoom factor. While its vertices were mapped in a continuous coordinate system, the polygon was subsequently converted into a collection of (discrete) image pixels. We did not map inclusions inside inclusions. Identification of inclusions was limited to the well-illuminated terrain in the foreground of the scene, an area we also outlined with a polygon. Inside this area, we defined matrix pixels as all those not associated with inclusions, applying a threshold to the radiance to exclude shadows. The area of each inclusion was calculated from the number of image pixels it covered, the instantaneous field of view (IFOV) of those pixels, the distance from the camera aperture to the surface, and the angle between the surface normal and the line connecting the aperture and

surface (emission angle). As such, the area is corrected to first order for projection effects, as inclusions seen from the side on a sloping surface are larger than they appear. The distance to the rock surface and local emission angle were estimated from the DTM in Scholten et al. (2019). The color-coded distance in Figure 7 shows that most of the rock in the foreground is roughly at 25 cm. The distance to the rock in the background is not known accurately because of a lack of stereo coverage, but is certainly larger than 40 cm. Mapping was restricted to inclusions on terrain closer than this distance. The surface recedes in an apparent hollow at the bottom right of the scene and is therefore out of focus. The uncertainty of the DTM is about 0.5 cm in the foreground at a distance of 20 cm and about 1.5 cm at a distance of 30–40 cm (Scholten et al. 2019). Figure 7 also shows the phase angle of illumination by the LEDs. The phase angle is generally low, around 5° for the well-illuminated surface in the foreground. The low phase angle ensures that we can actually distinguish the inclusions, unobscured by the strong shadows that characterize the day images of this rough surface. The phase angle decreases with distance from the camera, so it is smaller for the poorly illuminated terrain in the back and the hollow at bottom right. The phase angle was calculated on the assumption of illumination by a point source at the center of the LED array. In reality, any point of the surface received light with a variety of phase angles due to the extended size of the array ($4.2 \times 0.9 \text{ cm}^2$). For example, the edges of the array illuminated the terrain in the foreground with a phase angle that was different by about 5° from the point-source estimate.

Mapping ambiguities arose because of unclear boundaries and spectral variations within apparent inclusions. To illustrate these challenges, we enlarge the area in the foreground at the bottom of the frame in Figure 8 in which several features are highlighted. Feature 1 appears to be an inclusion with clear boundaries. However, it harbors pixels that appear either red or blue in the color composite, and its average color may therefore appear neutral. Feature 2 is a reddish inclusion whose boundaries are clearly defined in the color composite in (a) but it appears to be larger in the stretched composite in (b). Feature 3 was mapped as a collection of three inclusions, one of which is clearly redder than the others. But one could arguably draw an outline around the entire group to count it as a single inclusion. Feature 4 is marked as an inclusion on the basis of its slightly brighter appearance, but its boundaries are so indistinct that this feature might as well be an expression of local topography. Finally, the matrix in (b) (i.e., pixels that are

⁵ <https://www.esri.com/en-us/arcgis/about-arcgis/overview>

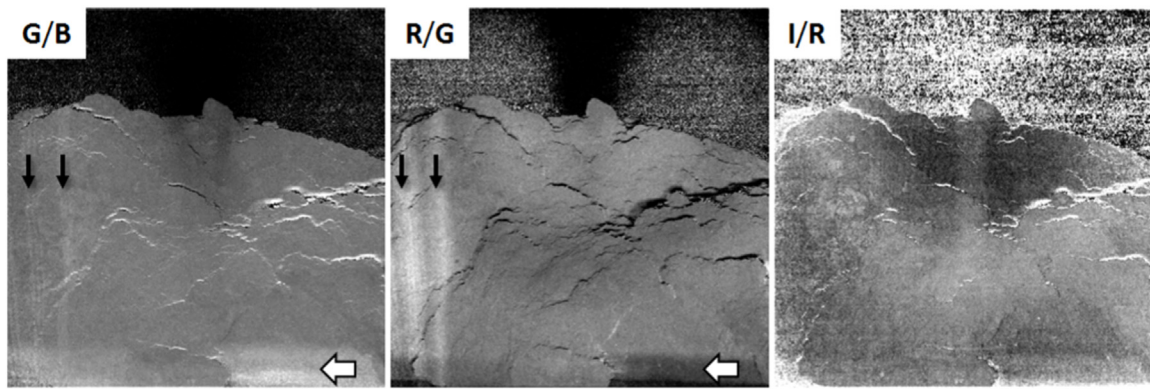


Figure 6. Artifacts in color ratio frames of set 14: vertical red stripes (black arrows), a horizontal green bar (white arrows), and a dark center for I/R . The frames are displayed with a similar brightness stretch.

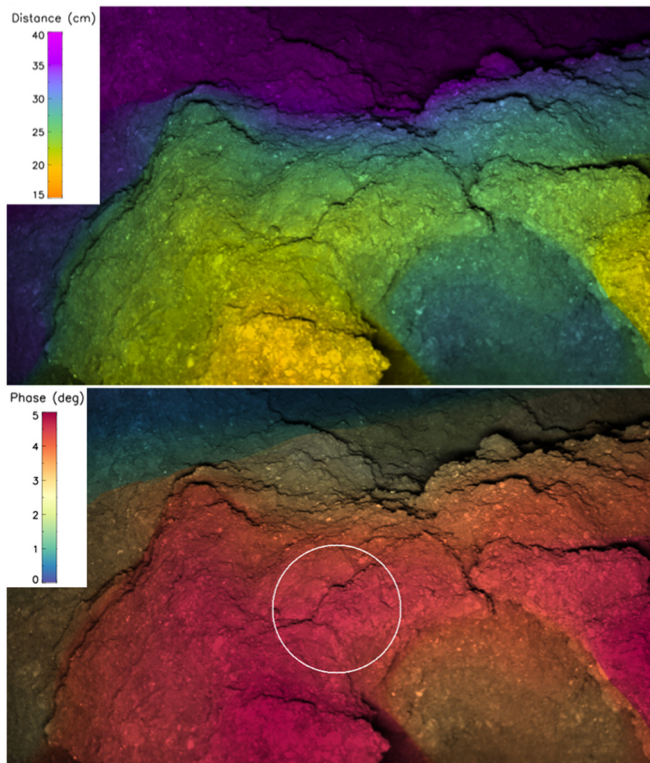


Figure 7. Distance from the camera aperture to the surface (top) and illumination phase angle (bottom) were calculated from the DTM in Scholten et al. (2019). The phase angle calculation assumes illumination by a point source at the center of the LED array. The average distance and phase angle inside the circle are 23.6 ± 1.0 cm and $4.5^\circ \pm 0.1^\circ$, respectively. The maximum phase angle in the foreground is 5.02° .

not marked red) contains abundant small areas that are brighter than their surroundings. In fact, they are so abundant that one suspects that what we have defined as the “matrix” is not a homogenous substance. These examples make it clear that the “inclusions” that we refer to in this report are not uniquely defined.

3. Results

3.1. Rock Reflectance

We derived the absolute reflectance (I/F) of the Ryugu rock by photometrically correcting the G image through Equation (2). Figure 9 shows both the uncorrected (radiance)

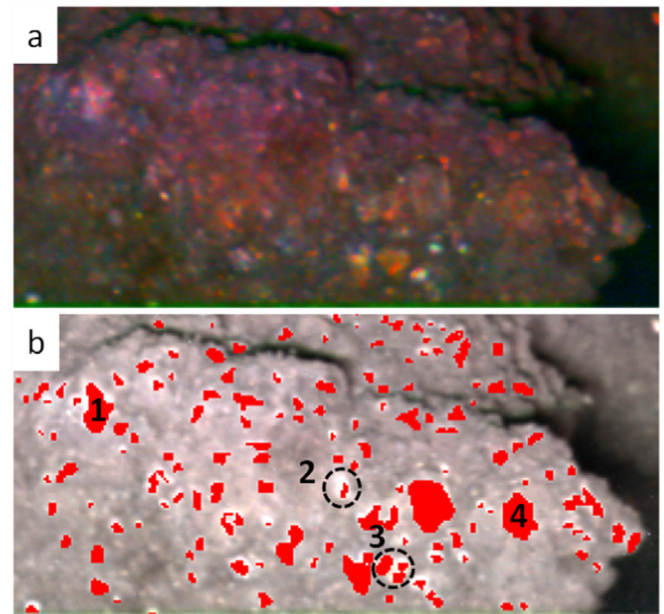


Figure 8. Challenges associated with mapping of inclusions. The area shown is located at the bottom of the frame. (a) Saturated (R, G, B) composite at full brightness range with red intensity reduced. (b) Corresponding map with inclusions marked in red on a stretched color composite background. Features labeled 1–4 are discussed in the text.

image and the corrected (reflectance) image. Because the DTM is increasingly uncertain beyond 35 cm, we restrict the correction to that distance. The brightness in the reflectance image is much more evenly distributed over the frame than in the radiance image, indicating a successful photometric correction (assuming that the rock reflectance is uniform). For example, the hollow in the foreground is no longer recognizable as such. The reflectance increases toward the terrain in the background, consistent with the lower average phase angle there (see Figure 7). We calculate the average reflectance for the terrain inside the circle in Figure 9 as $\bar{r}_F = 0.034 \pm 0.006$ at an average phase angle of $4.5^\circ \pm 0.1^\circ$. The circle was chosen such that it enclosed terrain that is comparatively free of image artifacts (see Figure 6) and is large yet small enough such that the phase angle does not vary by too much. While the standard deviation of the reflectance of the pixels inside the circle is 0.006, the true uncertainty of this estimate of the rock reflectance is smaller. It is derived from the uncertainty of the green responsivity factor (1%, Table 3),

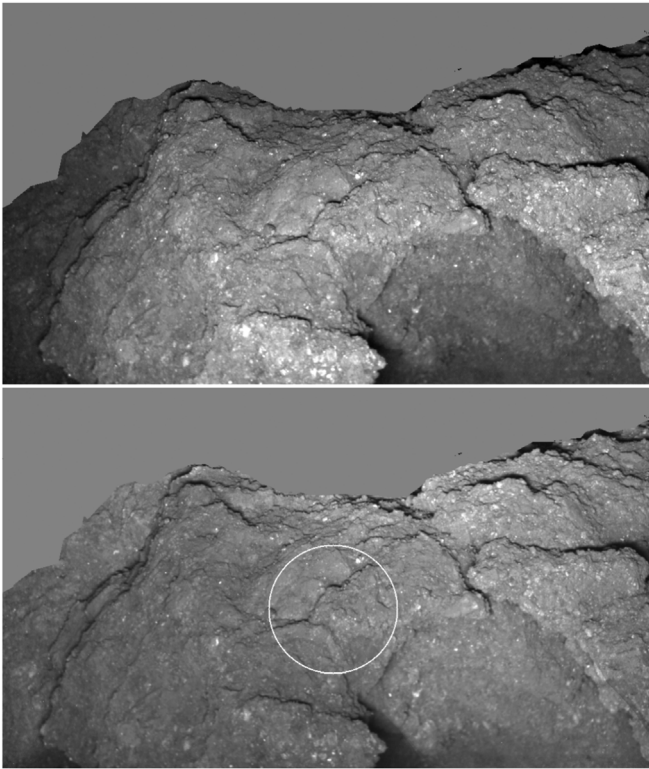


Figure 9. Photometric correction of the green image for terrain closer than 35 cm to the aperture. Top: radiance image G. Bottom: reflectance image. The average reflectance inside the circle is $\bar{r}_F = 0.034 \pm 0.006$.

variations in the irradiance image J (5%, Figure 3), and uncertainty in the distance to the rock in the DTM. The distance to the area in the circle is about 25 cm (Figure 7), for which the uncertainty is about 1 cm, or 4% (Scholten et al. 2019). Adding up these percentages, we arrive at a total uncertainty of 10% and estimate the reflectance of the Ryugu rock in the green channel as $r_F = 0.034 \pm 0.003$ at a 4.5° phase angle. We can predict the reflectance of the average Ryugu surface for a phase angle of 4.5° using the photometric model parameters from Sugita et al. (2019), which agree with those of Ishiguro et al. (2014) and are valid for the Optical Navigation Camera (ONC) v -band at 549 ± 14 nm (Kameda et al. 2017). The predicted I/F values for the $(\iota, \epsilon) = (4.5^\circ, 0^\circ)$, $(2.2^\circ, 2.3^\circ)$, and $(0^\circ, 4.5^\circ)$ geometries are all equal to 0.036° , which agrees very well with our reconstructed I/F of 0.034 ± 0.003 at 532_{-24}^{+12} nm. Thus, from a photometric point of view, the rock in front of MASCOT is typical for Ryugu.

The reconstructed reflectance spectrum of the Ryugu rock is shown in Figure 10. The mean reflectance is that of the pixels inside the circle in Figure 9, with the blue vertical error bars indicating the standard deviation. The sizes of the error bars reflect the brightness variations over the terrain, which includes shadows, but not the uncertainty of the spectral shape. The latter is the uncertainty of the spectral calibration, which derives from the uncertainty of the responsivity factors (only 1%) and that of the LED irradiance in the different color channels. The (spectral) uncertainty in the LED irradiance dominates the calibration uncertainty and concerns the color correction, i.e., division by the color ratio frames in Figure 3. As these frames are scene-dependent, their uncertainty is difficult to quantify. For example, frame V_3 was constructed

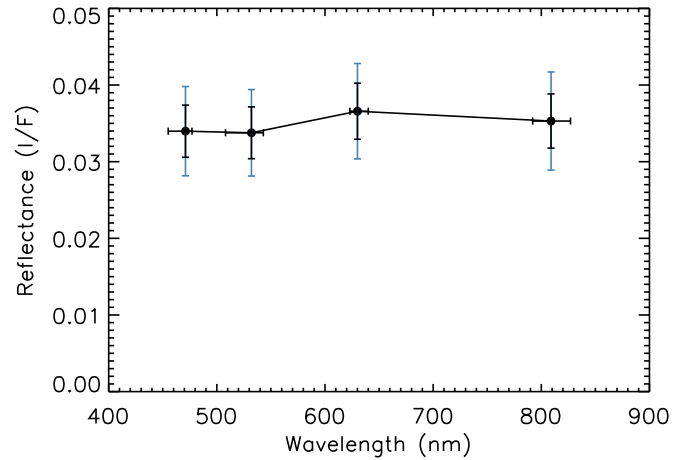


Figure 10. Absolute reflectance of the Ryugu rock, defined as the average of the image pixels inside the circle in Figure 9 and valid for a phase angle of $4.5^\circ \pm 0.1^\circ$. The blue error bars indicate the standard deviation of the pixels whereas the black error bars provide the uncertainty of the spectral calibration.

from images of a flat plate and has large-scale variations of around 15%. The uncertainty of the color correction is probably smaller than that. We adopted an uncertainty of 10% for the black vertical error bars on the rock reflectance spectrum in Figure 10. Within this uncertainty, our spectrum is consistent with average reflectance spectra of Ryugu from ONC images (Sugita et al. 2019). The slight excess of the MASCam reflectance in the red channel is not necessarily real as it is within the calibration uncertainty.

3.2. Inclusions

3.2.1. Spatial Distribution

We mapped a total of 1443 inclusions inside an area that was well illuminated due to its proximity to the camera. The totality of this area minus inclusions is defined as the matrix, where we applied a lower threshold of $0.008 \text{ W m}^{-2} \text{ sr}^{-1}$ to the radiance (for all LED colors) to exclude areas in shadow. A map of the inclusions and matrix pixels is shown in Figure 11. The inclusions appear to be more or less uniformly distributed over the mapping area. We tried to estimate the total area covered by the inclusions and the matrix to estimate their respective volume abundances, which are thought to be diagnostic quantities. However, we found the total matrix area to be dominated by pixels with an emission angle close to 90° . The area derived for such pixels is probably very inaccurate. The resolution of the Scholten et al. (2019) DTM appears to be much lower than the actual scale of the surface roughness so the emission angle calculated for image pixels is generally only a first-order approximation. We therefore selected only matrix pixels with an emission angle smaller than 80° (excludes 1.4%). The total area of the matrix pixels is then 172 cm^2 . For the same reason, we selected only inclusions with an average emission angle smaller than 80° (excludes 6). The total area of the mapped inclusions is then 13.6 cm^2 . The areal abundance of inclusions is $100\% \times 13.6 / (13.6 + 172) = 7.3\%$, which corresponds to a matrix areal abundance of 92.4%. As a test, we also estimated the pixel areas without the correction for emission angle and found inclusion and matrix abundances of 7.2% and 92.8%, respectively. These values are virtually identical to the earlier ones, implying that the retrieved

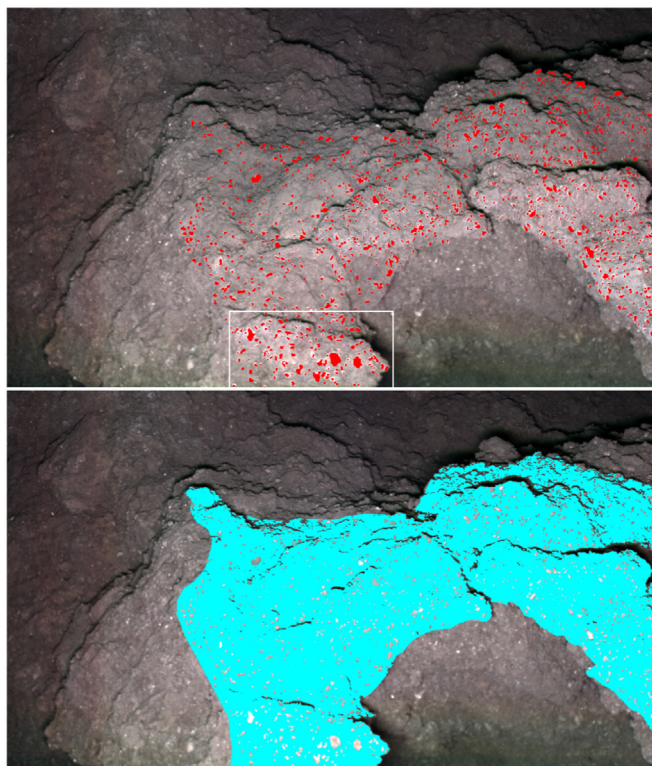


Figure 11. Definition of inclusions and matrix. Top: inclusion pixels (red). The area in the rectangle is enlarged in Figure 8. Bottom: matrix pixels (cyan).

abundances are robust. However, the terrain we mapped as the “matrix” may include unresolved inclusions, so our inclusion and matrix abundances are lower and upper limits, respectively. Finally, we performed a simple numerical simulation of small, randomly distributed spheres throughout a volume and verified that the volume abundance (vol%) can be estimated as the observed areal abundance on a planar surface. Thus, to first order, the volume abundance is equal to the retrieved areal abundance.

3.2.2. Spectral Properties

The color of the inclusions can be determined as the ratio of the color-corrected radiance images and thus does not depend on an accurate determination of the LED irradiance. We investigate the color of the inclusions as defined in Figure 11. We determined the average spectrum of each inclusion and subjected the body of spectra ($n = 1441$) to a principal component analysis (PCA) using the `prcomp` package in R.⁶ The first three principal components (or eigenvectors) are shown in Figure 12, where we omitted the last component (PC4) as the highest components generally contain only noise. PC1 represents the average shape of the inclusion spectra, which is similar to the average spectrum of the rock itself (Figure 10). PC2 represents the dominant color variation, which in this case is a change in the spectral slope from blue to infrared, while PC3 expresses more subtle color variations that may exist in addition to the slope variation. The contribution of the three components to the variance is PC1: 97.9%, PC2: 1.4%, and PC3: 0.5%. The large contribution of PC1 is the consequence of the variable degree of illumination over the scene, where inclusions in the background are perceived as darker than those in the foreground. The dominant

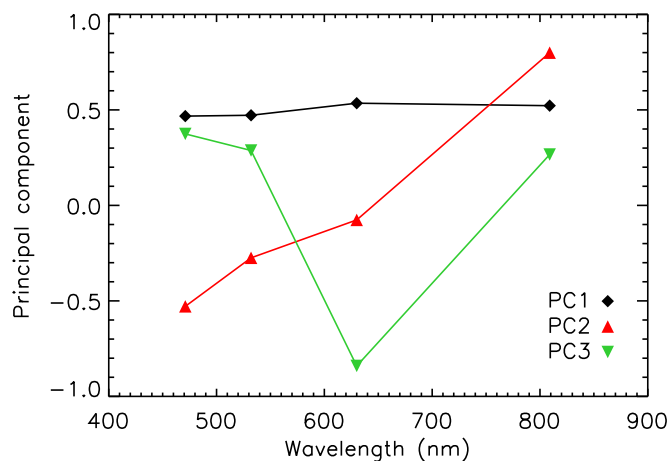


Figure 12. Principal components of the inclusion spectra. The contribution of the three components to the variance is PC1: 97.9%, PC2: 1.4%, and PC3: 0.5%.

spectral variation (PC2) is therefore a change in spectral slope over the entire wavelength range of the LEDs. PC3 uncovers a possible variation in the red channel with respect to the other three, which may be related to red being slightly depressed in PC2. To better understand this variation, we evaluate the spectra of several individual inclusions. Many inclusions have a single pixel at their center that is much brighter than the others, indicating that they are unresolved, in which case the image merely represents the point-spread function (PSF) of the imaging system. We therefore focus only on that brightest pixel. To circumvent the uncertainties associated with unequal illumination patterns between the LEDs, we calculate the ratio of the radiance in the brightest pixel and the average radiance of the matrix, chosen as a (circular) area of uniform appearance in close proximity. Figure 13 shows the ratio spectra of 14 prominent inclusions, labeled *a-n*. Some of these are outside the terrain mapped earlier, as, in this case, the selection criterion is radiometric accuracy (lack of image artifacts) rather than DTM accuracy. We calculated ratio spectra for each of the image sets 13, 14, and 15 (Table 1) and the ratio spectra in the figure are averages over these three sets. A few inclusions (*a*, *b*, *d*) are very bright and very red. Inclusion *a* is the most extreme case, being more than 8 times brighter than the matrix in the infrared. Another inclusion (*h*) is also much brighter (by about a factor of 4) but blue instead. Other inclusions are typically twice as bright as the matrix, and either red, blue, or spectrally neutral. Variation in the red channel indeed exists. The radiance in the red channel appears to be reduced for inclusions *c*, *e*, and *j*, although the error bars are relatively large and may be slightly enhanced for inclusions *i* and *m*.

We return to the inclusions as they are mapped in Figure 11. We express the dominant color variation with a single quantity: the relative spectral slope. In light of the lack of apparent artifacts in the mapping area in the G/B ratio frame in Figure 6 and the “flat” appearance of the rock, we define the relative slope as $(G - B)/B$. Figure 14 shows the relative slope as a function of inclusion area. The matrix pixels are neutral in color with a relative spectral slope of -0.003 ± 0.028 . We now define “red” inclusions as those with a spectral slope larger than the average spectral slope of the matrix pixels plus one standard deviation and “blue” inclusions as those with a slope smaller than the average matrix slope minus one standard deviation. The figure shows that the vast majority of inclusions have spectral slopes

⁶ <https://www.r-project.org>

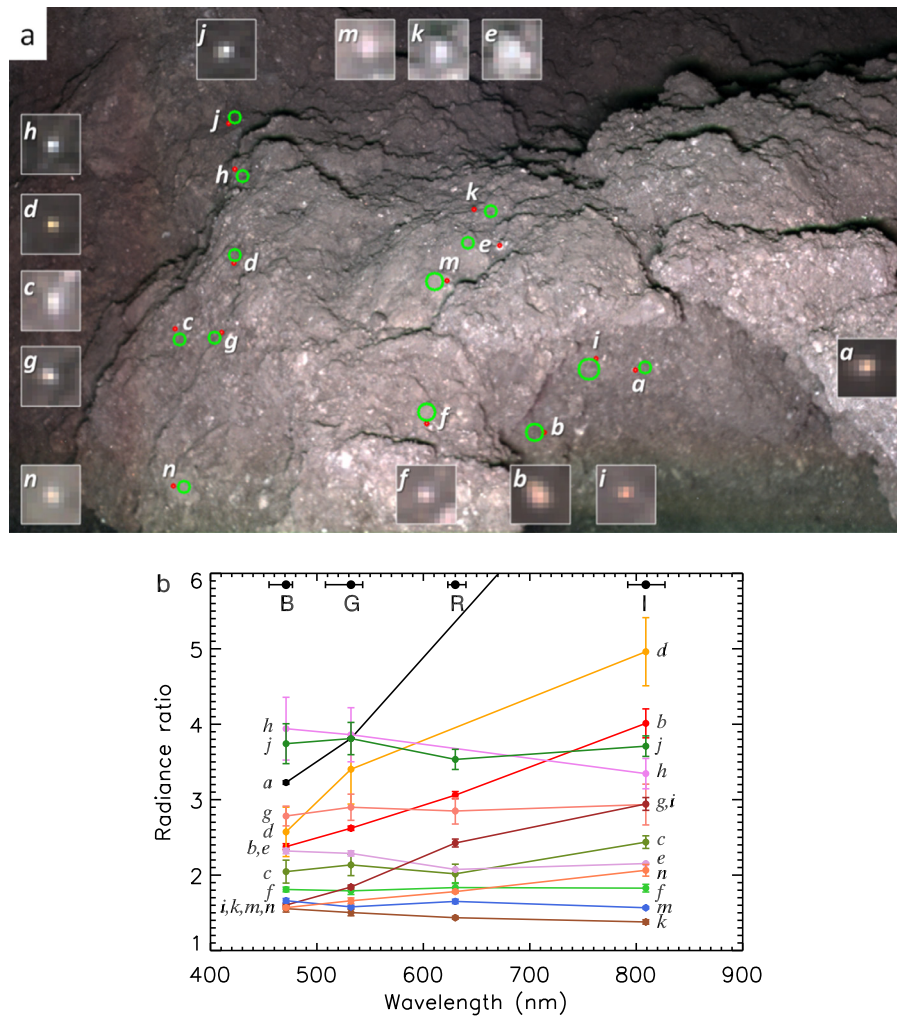


Figure 13. Inclusion spectral diversity. (a) Map of selected inclusions, labeled *a-n*. The red circles indicate the inclusion locations whereas the green circles indicate nearby featureless matrix areas. The insets are (*R, G, B*) composites at full brightness range (zero is black). The inclusion radiance was determined for the pixel at the center of the inset. (b) Ratio spectra of all labeled inclusions, calculated as the radiance of the central pixel divided by the average radiance of the associated matrix. Each data point is the radiance ratio for that pixel averaged over the image sets 13, 14, and 15 ($n = 3$), with the error bars indicating the standard deviation. Name and wavelength range of the color channels are indicated at the top. The red (*R*) data point is missing for some inclusions because of overexposure. The infrared (*I*) ratio for inclusion *a* plots outside the range as 8.2 ± 0.3 .

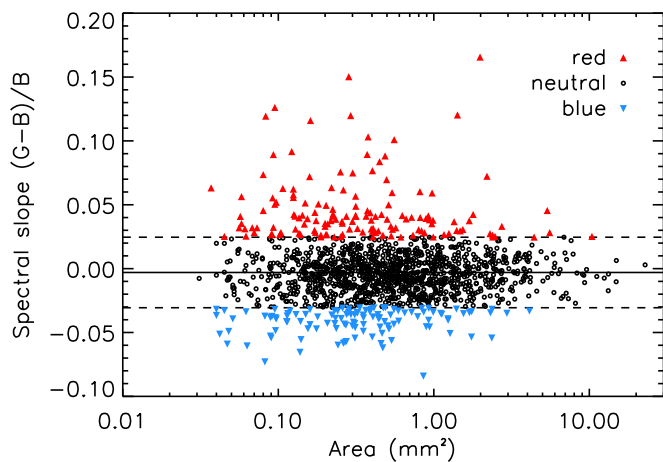


Figure 14. The relative spectral slope, defined as $(G - B)/B$, of all mapped inclusions as a function of inclusion area. The drawn line is the average spectral slope of the matrix pixels, with the dashed lines indicating the standard deviation. We define “red” inclusions as those with a spectral slope larger than the upper dashed line and “blue” inclusions as those with a slope smaller than the lower dashed line.

that are in the range of those of the matrix pixels. This suggests that the matrix harbors unresolved or otherwise unrecognized inclusions. Also, some inclusions harbor both red and blue pixels (examples in Figure 8), which tends to reduce their average spectral slope to that of the matrix. The number of red inclusions is 1.2 times larger than the number of blue inclusions. This ratio is within the expected uncertainty assuming Poisson statistics, so the number of red and blue inclusions is not significantly different. However, the ratio of red over blue inclusions critically depends on the definition of spectral slope; had we defined the slope as $(R - B)/B$ or $(I - B)/B$, the ratio would be 1.4 and 4.5, respectively. Figure 14 also reveals that inclusion color is not a matter of size, although the largest inclusions in our sample ($>3 \text{ mm}^2$) are strictly neutral in color, perhaps as a result of averaging any spectral diversity inside. Finally, we counted nine very red inclusions (slope > 0.1), but none that are similarly blue (slope < -0.1).

3.2.3. Size Distribution

The smallest and largest inclusions in our sample have an area of 0.031 and 23 mm^2 , respectively. The size distribution

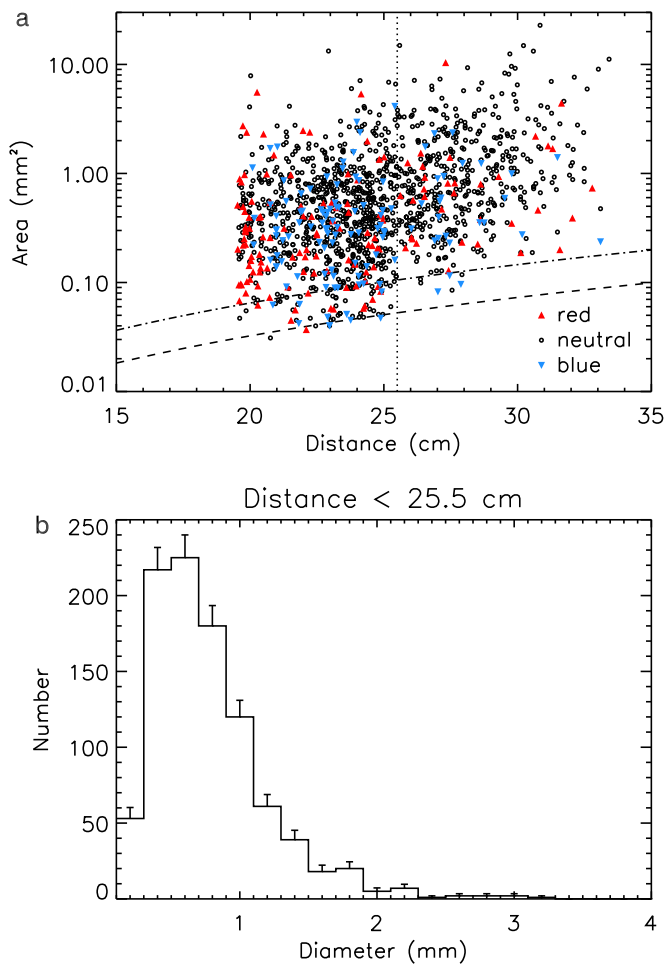


Figure 15. Inclusion size distribution, with inclusion color defined in Figure 14. (a) Projected inclusion area as a function of distance from the aperture. The dashed line corresponds to the area covered by a single pixel with an IFOV of 0.9 mrad whereas the dashed-dotted line corresponds to the area covered by two such pixels. The space between the two lines represents a sampling gap. Inclusions left of the dotted line were selected for the histogram. (b) Histogram of the inclusion diameter defined for a disk of identical area with Poisson error bars. The counts include inclusions only on terrain closer than 25.5 cm ($n = 954$). There is one inclusion with a diameter larger than 4 mm.

of the mapped inclusions is affected by three biases. Bias (1) is that the smallest inclusions can only be distinguished on terrain closest to the camera. Figure 15(a) shows the inclusion area as a function of distance to the camera aperture. It shows that inclusions were mapped on terrain at a distance between 19 and 34 cm. The dashed curve represents the area of a single pixel with an IFOV of 0.9 mrad seen face-on (zero emission angle) as a function of distance. The smallest inclusions cluster around this curve, indicating that their size is a single pixel. We cannot be sure that such inclusions are fully resolved, so their area is an upper limit. Another curve (dashed-dotted) represents inclusions that cover an area of two image pixels. The mostly empty space between the curves is a sampling gap. Similar gaps exist for higher pixel numbers. Bias (2) is introduced by the sloping terrain at larger distance; the higher emission angles there make it impossible to see many small inclusions. Bias (3) follows from the fact that most of the area we mapped is at a larger distance so there we find a relatively large number of large inclusions. The three kinds of bias make it difficult to evaluate whether inclusions are uniformly distributed over the rock, i.e., independent of their size. At least when we

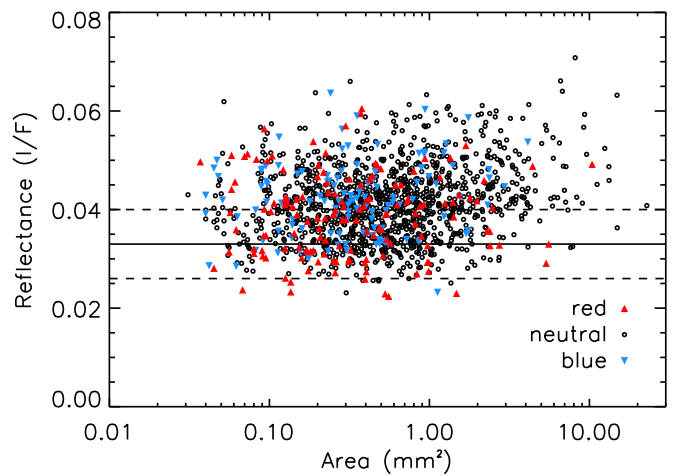


Figure 16. Absolute reflectance of the inclusions derived from the photometrically corrected G image, with inclusion color as defined in Figure 14. The drawn line is the average reflectance of the matrix pixels, with the dashed lines indicating the standard deviation. The average phase angle of all inclusions is $4.6^\circ \pm 0.5^\circ$.

distinguish red and blue inclusions, again defining the relative slope as $(G - B)/B$, we find little variation; both red and blue inclusions are found at any distance. However, if we define the relative spectral slope as $(R - B)/B$, there appear to be more blue than red inclusions at a larger distance. The distribution is uniform again for $(I - B)/B$, so the odd result for the red channel may reflect heterogeneity in the rock but could also be an artifact.

The three biases make it necessary to restrict the size analysis to inclusions mapped on terrain relatively close to the camera. It appears that single-pixel-sized inclusions were only recognized up to a distance of 25.5 cm (dotted vertical line in Figure 15(a)), so we adopt this as a distance limit. Inclusion size is often reported in the literature as the diameter of a sphere. We therefore convert our inclusion area a into diameter $d = 2\sqrt{a/\pi}$ of an equivalent disk. Figure 15(b) shows a histogram of the diameter of inclusions closer than 25.5 cm. The minimum and maximum diameter in the sample are 0.20 and 5.4 mm, respectively. The vast majority of inclusions is smaller than 1 mm in diameter and very few are larger than 2 mm. The histogram peaks around 0.5 mm diameter. However, the number in the smallest size bin (0.1–0.3 mm) is uncertain for two reasons. First, the area of a single pixel with an IFOV of 0.9 mrad seen face-on at a 20 cm distance corresponds to $d = 0.20$ mm. Thus, some inclusions assigned to this bin could actually be smaller than 0.1 mm, but so bright that they appeared bigger due to the detector’s PSF. On the other hand, the rock displays many small, faint brightness features (see examples in Figure 8), which we assumed to be photometric variations resulting from topography, but might also be inclusions of the correct size that were too faint to be recognized. As there are competing biases for the number in the smallest size bin, it is probably not too far off and the peak in the size distribution around 0.5 mm is likely real.

3.2.4. Brightness Distribution

The successful photometric correction described in Section 3.1 allows us to reconstruct the absolute reflectance of the inclusions. Inclusions generally appear bright in the images and we did not unequivocally identify any that are

darker. Figure 16 compares the reflectance of the inclusions with the average matrix reflectance, again distinguishing red and blue inclusions as defined in Figure 14. The figure confirms our impression that inclusions are generally brighter, by up to a factor of two, than the matrix at phase angles of around 5° . The brightness of inclusions seems to depend on neither color nor size.

4. Discussion

In the previous sections we determined the reflective properties of the Ryugu rock and its inclusions and derived the size distribution for the latter. Our results suggest that the rock is typical for Ryugu, although this should be confirmed by an analysis of Hayabusa2 observations of the landing site.⁷ We should now be in a position to choose the most appropriate CC analog group for Ryugu rocks from the perspective of MASCam. The low albedo over the entire visible wavelength range poses a challenge to match Ryugu with any CC group (Sugita et al. 2019), so we will search for clues in the inclusion size distribution and their spectrophotometric properties.

Inclusions in the Ryugu rock appear to be exclusively brighter than the surrounding matrix. A principal component analysis (PCA) reveals that their dominant spectral variability is a variation in visible spectral slope, with an additional, more subtle, spectral variation existing around $0.63 \mu\text{m}$, as expressed by PC3 (Figure 12). The shape of our PC3 is reminiscent of that of PC3 in a PCA of visible spectra of CCs in Hiroi et al. (2017). The authors linked a depression in their PC3 at $0.7 \mu\text{m}$ to variability in the $0.7 \mu\text{m}$ absorption band, which is attributed to Fe^{2+} - Fe^{3+} charge transfer in hydrated phyllosilicates like serpentines and saponites (Vilas & Gaffey 1989; Cloutis et al. 2011a). It is tempting to attribute the shape of our PC3 to the presence of this absorption band in the spectrum of some inclusions but there are several complicating factors. First, the higher PCs are usually affected, or even dominated, by noise. Second, the Hiroi et al. (2017) PCA was for a variety of CCs, whereas ours is for a variety of inclusions inside a single, putative CC. Third, the MASCam red channel is centered at $0.63 \mu\text{m}$, which may not be deep enough into the (broad) $0.7 \mu\text{m}$ band for a positive identification. Confirming the presence of the $0.7 \mu\text{m}$ band in inclusion spectra would have important implications. The spectrum of the rock as a whole is consistent with that of the Ryugu average (Figure 10). It does not show this band, meaning that the matrix does not either. Sugita et al. (2019) and Kitazato et al. (2019) argued that the closest meteorite analogs for Ryugu are heated CCs. If some inclusions display the $0.7 \mu\text{m}$ band, the implication of their argument is that the rock matrix was heated but the inclusions were not. Such a sequence of events is difficult to envision.

Ideally, we put these results in the context of other studies of CC inclusion color variability in the visible wavelength range. Unfortunately, such studies appear to be scarce, probably because spectral features diagnostic for the composition are generally located in the near-IR. Also, spectral studies commonly deal with CC powders but the images of the Ryugu rock are more akin to those of meteorite fragments or slabs. Reflectance spectra of CC slabs may be more blue-sloped and generally darker than spectra of powders (Cloutis et al. 2018). MASCam found Ryugu inclusions to be either blue (negative spectral slope) or red (positive slope). Enrichment in olivine

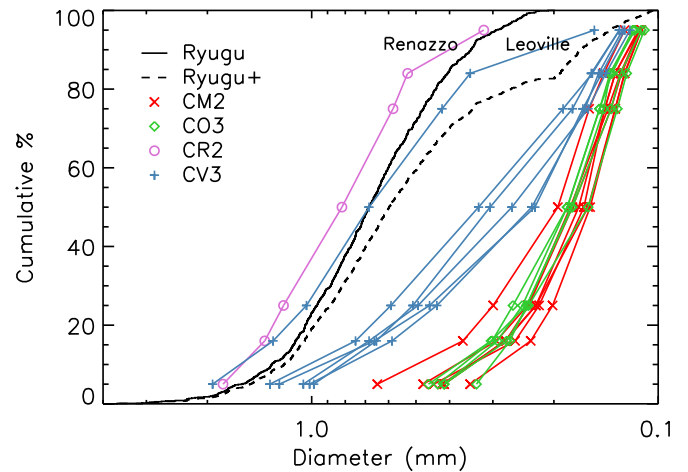


Figure 17. Cumulative size distribution of all inclusions mapped on the Ryugu rock at a distance < 25.5 cm compared to those of meteorites in different carbonaceous chondrite groups (King & King 1978). The dashed curve (“Ryugu+”) represents the Ryugu distribution with 200 additional inclusions with diameters randomly chosen between 0.1 and 0.2 mm. Two meteorite names are indicated.

appears to give rise to a blue spectral slope in the visible for bright inclusions in the Murchison meteorite (Green et al. 2015), which may also explain the color of blue Ryugu inclusions. Many Ryugu inclusions are red, some of them very red, which may hint at the presence of phyllosilicates, Fe-rich oxides, or spinel (Cloutis et al. 2011b; Green et al. 2015).

The smallest and largest inclusions have sizes consistent with those of chondrules and refractory inclusions in CC meteorites, respectively. These two groups are distinguished not only by their size but also the basis of their morphology, with chondrules being spherical and refractory inclusions generally having an irregular shape. Unfortunately, the limited resolution of the MASCam images prevents us from verifying the spherical nature of CCs. Thus, given the absence of morphological and compositional information, we cannot clearly distinguish between chondrules and refractory inclusions. The inclusion size distribution may be diagnostic for CC group membership. The presence of abundant inclusions in the Ryugu rock excludes the CI group as an analog candidate, as members of this group typically lack inclusions. King & King (1978) determined the size distribution of inclusions larger than 0.1 mm in 19 CC meteorites from four different groups (CM2, CO3, CR2, and CV3). The authors reported the inclusion maximum diameter as size parameter ϕ , which relates to diameter as $d = 2^{-\phi}$ mm (Folk & Ward 1957). We compare their measurements for all inclusions regardless of shape or (suspected) type to the Ryugu size distribution in Figure 17. The CM2 and CO3 size distributions mostly overlap in a relatively narrow range, with the vast majority of their inclusions being smaller than 0.5 mm. CV3 inclusions are typically larger than CM2/CO3 inclusions, on average by a factor of 2. The inclusions of two meteorites are considerably larger than those of the others: Renazzo (CR2) and Leoville (CV3). The former was classified as CV2 by King & King (1978), but is now considered a CR2 (Cloutis et al. 2012a). The Ryugu size distribution is close to these two meteorites, with a shape most similar to that of the Renazzo distribution. The King & King (1978) distributions are supposed to be complete down to 0.1 mm diameter, but we likely underestimate the number of the smallest inclusions in the Ryugu rock (see

⁷ A paper on this topic is in preparation.

Table 4

Matrix Abundance in the Ryugu Rock Compared to Estimates for Different CC Groups (King & King 1978)

	CM2	CO3	CR2	CV3	Ryugu
Matrix area%	93 ± 3 (7)	74 ± 9 (5)	48 (1)	58 ± 8 (6)	<93

Note. The number of meteorites on which the estimate is based is given in brackets.

Section 3.2.3). We therefore modified the Ryugu size distribution by adding 200 inclusions with a size between 0.1 and 0.2 mm, bringing the smallest size bin in the histogram in Figure 15(b) up to the level of its neighbor. Doing so changes the distribution curve only a little, merely bringing its shape into better agreement with that of Leoville. It appears that the similarity of the Ryugu size distribution to the Renazzo and Leoville distributions is robust, which implies that the rock's inclusions are rather large for a CC. We do not suggest that these two meteorites are good analogs for the Ryugu rock, as their density is too high (Corrigan et al. 1997).

Another diagnostic quantity is the inclusion abundance. We estimated that the areal abundance of small spherical inclusions is approximately equal to their volume abundance. We derived an inclusion abundance of around 7%, which means a matrix abundance of 93%. King & King (1978) also estimated the abundance of the matrix, defined as including particles smaller than 0.1 mm. Table 4 compares the Ryugu matrix abundance with that of the CC groups. The Ryugu abundance of 93% is an upper limit and agrees, in principle, with that of any group. However, the abundance is not likely to be underestimated by much, as the greatest uncertainty is associated with the number of smallest inclusions, which contribute only little to the area. The Ryugu matrix abundance therefore appears most similar to that of the CM2 group. The matrix abundance for the Renazzo and Leoville meteorites is 48% and 65%, respectively, considerably lower than that of the Ryugu rock. That said, it is not clear to what extent the size measurements of inclusions in MASCam images can be directly compared with the measurements on slabs of meteorite material by King & King (1978).⁸ We tentatively conclude that Ryugu inclusions are comparatively large, more similar to those associated with the CR2 and CV3 groups than the CM2 and CO3 groups. On the other hand, the matrix abundance is comparatively high, most similar to that seen in the CM2 group.

Lacking compositional information, the inclusion size distribution is not a sufficient criterion for group membership, and the implications of the observed inclusion color variations are unclear. Nevertheless, it appears that the Ryugu rock does not easily fit into any of the CC groups. ATCCs are plausible analogs because of their low reflectance (Cloutis et al. 2012b; Kitazato et al. 2019; Sugita et al. 2019). Unfortunately, the size distribution and spectrophotometric properties of their inclusions have not been systematically documented. The Tagish Lake meteorite is also considered a possible analog (Jaumann et al. 2019). Attractive properties are its low density and

⁸ To address the deficiencies in our analysis, we performed an experiment in which we imaged a number of CCs with a MASCam model. We will analyze these images in a similar way as the Ryugu rock in this paper so the results may be directly compared. As our sample includes many meteorites that were also analyzed by King & King (1978), we will be able to verify that our methods yield comparable size distributions. The results of this experiment will be reported separately.

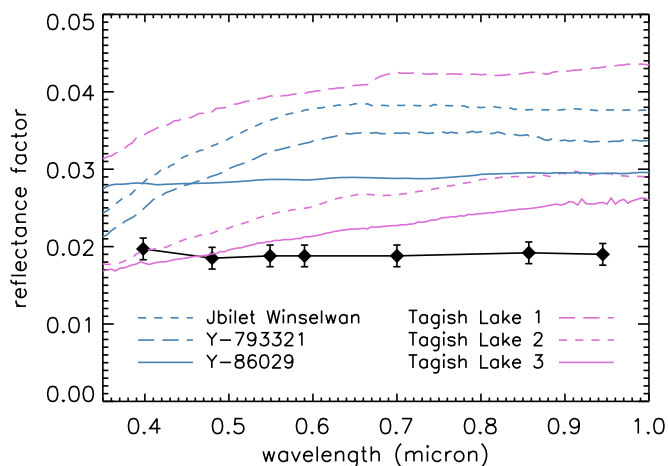


Figure 18. Reflectance spectra of three ATCCs and three Tagish Lake powder samples compared to that of Ryugu at the standard geometry of $(i, \epsilon, \alpha) = (30^\circ, 0^\circ, 30^\circ)$. The ATCC spectra (blue) are those in Figure 3 of Sugita et al. (2019). The Tagish Lake 3 spectrum is that in Figure 1 of the supplementary material of Hiroi et al. (2001). The Ryugu spectrum (black diamonds) is that in Figure 20 in Tatsumi et al. (2020). Details of the meteorite spectra are given in Table 5.

abundant inclusions (Hiroi et al. 2001; Zolensky et al. 2002). But is it also a good spectral analog? If we adopt the criterion of Sugita et al. (2019), a similarly low reflectance over the visible wavelength range, it is. In Figure 18 we compare the reflectance spectrum of three samples of Tagish Lake from the RELAB database⁹ (Table 5) with that of Ryugu and the three ATCCs shown in Figure 3(B) of Sugita et al. (2019). Tagish Lake spectrum #3 (Hiroi et al. 2001) is closer to the Ryugu spectrum than that of the ATCCs. The other two Tagish Lake spectra span the ATCC range. But spectrum #1 may have the highest overall reflectance because its sample was a pressed pellet. Pressing the surface is expected to increase the reflectance at the standard viewing geometry (e.g., Schröder et al. 2014). Spectral ambiguity also exists for the ATCCs: all spectra in Figure 18 are for particular samples. The particulate spectrum of Y-86029 is flat but a fragment of the same meteorite has a red spectral slope and is 30%–40% more reflective (Tatsumi et al. 2020). Meteorite fragments may be more representative for the Ryugu rock than powders but a spectrum for a Tagish Lake fragment is not available in RELAB. A detailed assessment of the 2.7 μm band is beyond the scope of this paper, but we do note that, for one Tagish Lake sample in RELAB,¹⁰ this band has a similar depth and shape as that of the heated Ivuna sample in Hiroi et al. (1996), which was adopted as the best match for Ryugu by Kitazato et al. (2019).

Meteorites with a reflectance as low as that of Ryugu are not common. Tagish Lake is unique and dark ATCCs appear to be relatively rare among the CCs. Nakamura (2005) identified 21 ATCCs among the CCs found on Antarctica prior to 1992, to which Cloutis et al. (2012b) added six more. The Meteoritical Bulletin Database¹¹ lists 346 Antarctic CCs found prior to 1992. These numbers imply an abundance of 8% for ATCCs in the pre-1992 Antarctic CC population. We can also approach

⁹ http://www.planetary.brown.edu/relabdocs/relab_disclaimer.htm

¹⁰ Sample MT-TXH-025-L0, spectrum BKR1MT025L0. We note that this sample was pressed, which may have affected the reflective properties of the particulate.

¹¹ <https://www.lpi.usra.edu/meteor/metbull.php>







Table 5
Details for RELAB Meteorite Spectra Shown in Figure 18




Name in Legend	Spectrum ID	Sample ID	Sample Condition
Jbilet Winselwan	C1MT312A	MT-DAK-312-A	Particulate, ground, sorted
Y-793321	C1MP131	MP-KHO-131	Chip
Y-86029	C3MP111	MP-TXH-111	Particulate, ground, dry-sieved
Tagish Lake 1	C1MT25L2	MT-TXH-025-L2	Particulate, pressed
Tagish Lake 2	C1MT237C	MT-S1S-237-C	Particulate, ground, dry-sieved
Tagish Lake 3	C2MT11	MT-MEZ-011	Particulate, ground, dry-sieved

the question of abundance in terms of meteorite mass. The 345 Antarctic CCs (one does not have its mass listed in the database) have a total mass of 49.56 kg, half of which derives from a single meteorite (Y-791717). The total mass of the 27 ATCCs is 4.90 kg, which represents 10% of the total mass. While ours is not a comprehensive assessment, these abundances suggest that ATCCs are relatively rare, with the caveats that many ATCCs may not yet have been recognized as such and that not all are as dark as Ryugu (Cloutis et al. 2012b). On the other hand, C-type asteroids as dark as Ryugu are common (Belskaya & Shevchenko 2000; Shevchenko & Belskaya 2010). In fact, all three spacecraft encounters with C-type asteroids have yielded similarly low geometric albedos in the visible: 0.047 ± 0.005 for 253 Mathilde (Clark et al. 1999), 0.045 ± 0.002 for Ryugu (Sugita et al. 2019), and 0.044 ± 0.002 for 101955 Bennu (Lauretta et al. 2019). If ATCCs are a good analog for low-albedo C-type asteroid material, we would expect them to be common. They may exist in abundance in space but not make it to Earth's surface. If this is so, then the apparent rarity of ATCCs and Tagish Lake's unique status are consistent with the idea that Ryugu-type meteorites are too fragile to survive atmospheric entry (Grott et al. 2019).

This study was supported by the JSPS International Planetary Network. This research utilizes spectra acquired by Takahiro Hiroi, Michael Zolensky, Katsuhito Ohtsuka, Carle Pieters, and David Kring with the NASA RELAB facility at Brown University. We thank two anonymous reviewers for their helpful comments. The recalibrated MASCAM images and associated calibration frames are available at <http://europlanet.dlr.de/Hayabusa2/MASCOT/index.html>.

ORCID iDs

Stefan Schröder  <https://orcid.org/0000-0003-0323-8324>
 Katharina Otto  <https://orcid.org/0000-0002-0675-1177>
 Nicole Schmitz  <https://orcid.org/0000-0001-6481-6189>
 Frank Scholten  <https://orcid.org/0000-0002-1430-9223>
 Stefano Mottola  <https://orcid.org/0000-0002-0457-3872>
 Alexander Koncz  <https://orcid.org/0000-0001-8231-1109>
 Ralf Jaumann  <https://orcid.org/0000-0002-9759-6597>

Tra-Mi Ho  <https://orcid.org/0000-0003-3378-3227>
 Hikaru Yabuta  <https://orcid.org/0000-0002-4625-5362>
 Seiji Sugita  <https://orcid.org/0000-0001-6076-3614>

References

- Belskaya, I. N., & Shevchenko, V. G. 2000, *Icar*, 147, 94
 Bibring, J. P., Hamm, V., Langevin, Y., et al. 2017, *SSRv*, 208, 401
 Clark, B. E., Veverka, J., Helfenstein, P., et al. 1999, *Icar*, 140, 53
 Cloutis, E. A., Hiroi, T., Gaffey, M. J., Alexander, C. M. O. D., & Mann, P. 2011a, *Icar*, 212, 180
 Cloutis, E. A., Hudon, P., Hiroi, T., & Gaffey, M. J. 2012a, *Icar*, 217, 389
 Cloutis, E. A., Hudon, P., Hiroi, T., & Gaffey, M. J. 2012b, *Icar*, 220, 586
 Cloutis, E. A., Hudon, P., Hiroi, T., Gaffey, M. J., & Mann, P. 2011b, *Icar*, 216, 309
 Cloutis, E. A., Hudon, P., Hiroi, T., Gaffey, M. J., & Mann, P. 2012c, *Icar*, 221, 984
 Cloutis, E. A., Pietrasz, V. B., Kiddell, C., et al. 2018, *Icar*, 305, 203
 Corrigan, C. M., Zolensky, M. E., Dahl, J., et al. 1997, *M&PS*, 32, 509
 Folk, R. L., & Ward, W. C. 1957, *JsedR*, 27, 3
 Green, R. O., Ehlmann, B. L., Fraeman, A. A., et al. 2015, Lunar and Planetary Science Conf., 46, 2154
 Grott, M., Knollenberg, J., Hamm, M., et al. 2019, *NatAs*, 3, 971
 Herčík, D., Auster, H.-U., Constantinescu, D., et al. 2020, *JGRE*, 125, e06035
 Hiroi, T., Milliken, R. E., Pieters, C. M., et al. 2017, Lunar and Planetary Science Conf., 48, 1086
 Hiroi, T., Pieters, C. M., Zolensky, M. E., & Prinz, M. 1996, Lunar and Planetary Science Conf., 27, 551
 Hiroi, T., Zolensky, M. E., & Pieters, C. M. 2001, *Sci*, 293, 2234
 Ho, T.-M., Baturkin, V., Grimm, C., et al. 2017, *SSRv*, 208, 339
 Ishiguro, M., Kuroda, D., Hasegawa, S., et al. 2014, *ApJ*, 792, 74
 Jaumann, R., Schmitz, N., Ho, T. M., et al. 2019, *Sci*, 365, 817
 Jaumann, R., Schmitz, N., Koncz, A., et al. 2017, *SSRv*, 208, 375
 Kameda, S., Suzuki, H., Takamatsu, T., et al. 2017, *SSRv*, 208, 17
 King, T. V. V., & King, E. A. 1978, *Metic*, 13, 47
 Kitazato, K., Milliken, R. E., Iwata, T., et al. 2019, *Sci*, 364, 272
 Lauretta, D. S., Dellagiustina, D. N., Bennett, C. A., et al. 2019, *Natur*, 568, 55
 Nakamura, T. 2005, *JMPeS*, 100, 260
 Okada, T., Fukuhara, T., Tanaka, S., et al. 2020, *Natur*, 579, 518
 Sawada, H., Okazaki, R., Tachibana, S., et al. 2017, *SSRv*, 208, 81
 Scholten, F., Preusker, F., Elgner, S., et al. 2019, *A&A*, 632, L5
 Schröder, S. E., Grynko, Y., Pommerol, A., et al. 2014, *Icar*, 239, 201
 Shevchenko, V. G., & Belskaya, I. N. 2010, in European Planetary Science Congress 2010, 738
 Sugita, S., Honda, R., Morota, T., et al. 2019, *Sci*, 364, 252
 Tatsumi, E., Domingue, D., Schröder, S., et al. 2020, *A&A*, 639, A83
 Vilas, F., & Gaffey, M. J. 1989, *Sci*, 246, 790
 Zolensky, M. E., Nakamura, K., Gounelle, M., et al. 2002, *M&PS*, 37, 737